THE JOURNAL OF Ammonia Energy

Available online at

jae.cardiffuniversitypress.org

ISSN **2752-7735**
The Journal of Ammonia Energy 01 (2023) 074–082

Cardiff University Press | Gwasg Prifysgol Caerdydd

Exploring the Effects of Swirl Intensity on NO Emission in Ammonia-Methane-Air Premixed Swirling Flames

Wang G[a*], Guiberti TF[a,b], Roberts WL[a,b]

[a]*Clean Combustion Research Center, King Abdullah University of Science and Technology (KAUST), Thuwal 23955-6900, Kingdom of Saudi Arabia*

[b]*Mechanical Engineering Program, Physical Science and Engineering Division, King Abdullah University of Science and Technology*

Abstract

The high emission of nitrogen oxides (NOx) is one of the major obstacles to the practical application of ammonia as a carbon-free fuel. Improving the flow distribution and structure has been demonstrated to achieve low NOx emissions. However, in comparison to hydrocarbon flames, the influence of swirl intensities on ammonia NOx emissions is still not well understood. This study builds upon previous research by further exploring the effects of swirl intensity on NO production in ammonia-methane-air premixed swirling flames. A new adjustable axial swirler was designed to achieve a wide range of swirl numbers. We measured flame morphology, NO emissions, and NO and OH planar laser-induced fluorescence (PLIF) images over extensive ranges of equivalence ratio and ammonia fraction. The study found that increasing the swirl number from 0.6 to 1.0 resulted in a more compact flame, with enhanced reactions in the corner recirculation zone. Varying the swirl number significantly alters the NO concentration in the exhaust gas. The concentration of NO was significantly reduced at an equivalence ratio of 0.90 and an ammonia fraction greater than 80%. NO/OH-PLIF indicated that NO was primarily formed in the main reaction zone, with NO-PLIF intensity in the post-flame zone almost remaining constant at different heights. The integrated intensities of NO and OH-PLIF were obtained at different heights above the nozzle. A positive linear correlation was observed between NO-PLIF plateau intensity and NO mole fraction. The increased heat loss to the wall at larger swirl intensities reduces the flame temperature in the main reaction zone, which inhibit the formation of OH radicals, ultimately resulting in low NO emissions.

Received: 29th Jan 23; Accepted: 18th April 23; Published: 4th July 23

Keywords: NOx emissions, NO-PLIF, adjustable axial swirler, turbulence-chemistry interaction, heat loss.

Introduction

Ammonia has garnered significant attention in recent times as a promising alternative fuel owing to its carbon-neutral nature [1, 2]. Compared with hydrogen, ammonia can be liquefied after pressurizing 10 atm at room temperature, which is very convenient for storage and transportation [2]. However, there are some challenges with using ammonia as a fuel. For example, compared to most hydrocarbon fuels, ammonia has lower reactivity, which makes it challenging to ignite and easy to blow out [3-5]. Additionally, the combustion of ammonia is also prone to producing a large amount of harmful nitric oxide (NO) through the fuel NOx route [6, 7]. Therefore, designing efficient and clean combustors fueled by ammonia requires the development of strategies to stabilize the flame and minimize NO emissions.

One strategy that has been explored is utilizing swirling flows to stabilize ammonia combustion. Swirl is a crucial aspect in the stabilization of flames in high-velocity gas flows [8, 9]. A high swirl number creates a central recirculation zone, which promotes mixing between fuel and air and provides a continuous ignition source [8, 10]. Utilizing swirling ammonia flames is a viable approach to stabilize ammonia combustion in practical combustors.

It has been found that altering the swirl intensity can significantly impact the NOx emissions in hydrocarbon flames. Claypole and Syred [11] observed that the formation of NOx in natural gas swirling flames occurs primarily in the flame front, with the recirculation zone not contributing to NOx formation as the swirl numbers increase from 0.63 to 3.04. Zhou et al. [12] found that as the swirl number increases from 0 to 1, there is a nonmonotonic variation of NO in methane/air flames. Thermal NO is primarily influenced by temperature, whereas fuel NO is primarily influenced by species mixing via turbulence. Rashwan [13] found that increasing the swirl number can reduce the thermal NOx by 95% in non-

* Corresponding author. Email: guoqing.wang@kaust.edu.sa
https://doi.org/10.18573/jae.14

premixed methane flames, which can be attributed to the increase in mixing levels of the combustible mixture, thereby reducing the combustion temperature. Hosseini [14] found a similar trend: increasing the swirl number enhances the fuel-air mixing rate and reduces the high-temperature concentration points, significantly reducing the nitrogen oxide pollutants.

As mentioned above, most experimental and numerical studies focus on methane swirling flames. Recently, a few studies have investigated the effects of swirl intensities on NOx emissions of swirling flames burning ammonia blends [15]. A study in [16] observed that increasing the swirl number of premixed methane-air swirl flames with 2.5 and 5% ammonia additions resulted in larger NO formation for the smaller swirl intensity case.

This study builds upon previous research by further exploring the effects of swirl intensity on NOx production in ammonia flames. A bespoke single-stage swirl burner constructed in [17] was used to investigate the emission characteristics of ammonia-methane-air premixed swirling flames at elevated pressure. Planar laser-induced fluorescence (PLIF) of NO and OH was used to examine NO formation, which typically makes up ~90% of the NOx emission [18]. This method allows for the visualization of both NO and OH radicals, which are important intermediates in the formation of NOx in ammonia flames.

Experimental Setup and Methods

Experimental setup

Swirl burner with adjustable axial swirler

Experimental measurements of ammonia-methane-air swirling flame were conducted in the high pressure combustion duct (HPCD) at KAUST [19]. The design of the swirl burner and diagnostic methods are outlined in [17]. Briefly, a bespoke single-stage swirl burner was used to stabilize premixed ammonia-methane-air swirling flames at an absolute pressure of 2 bar. The swirling flow was generated by an axial swirler and confined within a cylindrical quartz tube with an inner diameter of 71 mm and a length of 360 mm. The bulk flow rate was kept at 200 SLM.

An adjustable axial swirler was designed for this study [17] to adjust the swirl number precisely. The detailed design of the adjustable axial swirler is depicted in Fig. 1. It comprises a fixed flange, a vane-supporting flange with 12 rotatable vanes, a drive flange, and a central rod. The thickness of the vanes is 0.5 mm. The angle (θ) between the vanes and the axis of the burner can be adjusted by rotating the vanes. Synchronized adjustments of all vanes were facilitated by the design, featuring 12 upright columns on both the fixed flange and drive flange, which resist the vane arm. By rotating the top rotating flange, all vanes are driven by the columns until the top and bottom columns clamp the vanes. Once the desired θ is achieved, the locking screws are tightened to secure the swirler. The swirl number is fixed at the setpoint. The vane angle can be adjusted from -76° to 76° to generate either clockwise or counter-clockwise swirling flows. The manufactured swirler and its drawings are illustrated in Fig. 1.

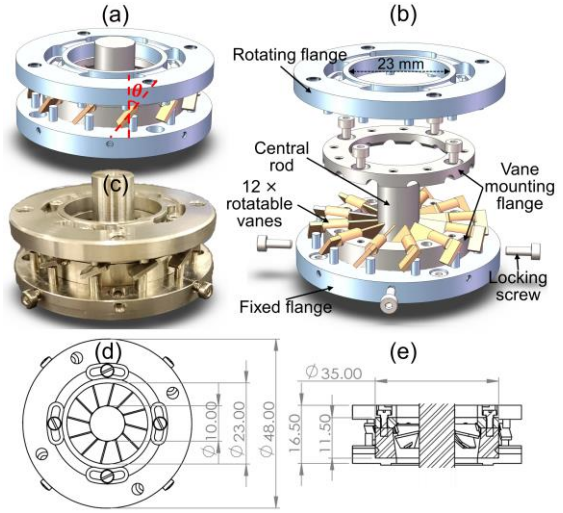

Fig. 1. The adjustable axial swirler with 12 rotatable flat vanes. (a) Three-dimensional design drawing, (b) exploded view of the swirler for rotating all the vanes synchronously, (c) a picture of the manufactured swirler, (d) the top view drawing, and (e) the central section view drawing.

According to the literature [20, 21], the swirl number is defined as

$$S = \frac{G_\theta}{R G_y} = \frac{\int_0^R \rho v_y v_\theta r^2 dr}{R \int_0^R [\rho v_y{}^2 + (p - p_\infty)] r dr} \quad (1)$$

Where G_y and G_θ are the axial fluxes of axial momentum and tangential momentum, respectively. R is the inner radius of the injector. ρ is the gas density. v_y and v_θ are the axial and tangential velocity components at radius r, respectively. $p - p_\infty$ is the relative pressure difference between the swirling jet and fluid at rest. According to the definition of swirl number, a simple algebraic expression of axial swirler can be derived under the assumption of uniform axial and tangential velocities [22],

$$S_A = \frac{2}{3}\left[\frac{1 - (D_i/D_o)^3}{1 - (D_i/D_o)^2}\right] \tan\theta \quad (2)$$

where D_i and D_o are the diameter of the central rod and the inner diameter of the swirler, respectively.

D_i/D_o is always less than unity. Equation (2) is employed to estimate the swirl number of the adjustable axial swirler. The corresponding algebraic swirl number (S_A), as shown in Fig. 2, increases from 0 to 2.9 as the vane angle increases from 0° to 76°. However, it should be noted that the axial swirler exhibits low efficiency and a high loss coefficient when the swirl number exceeds 0.8 [22]. This implies that the actual swirl number may not be as high as the steeply ascending curve at large θ in Fig. 2.

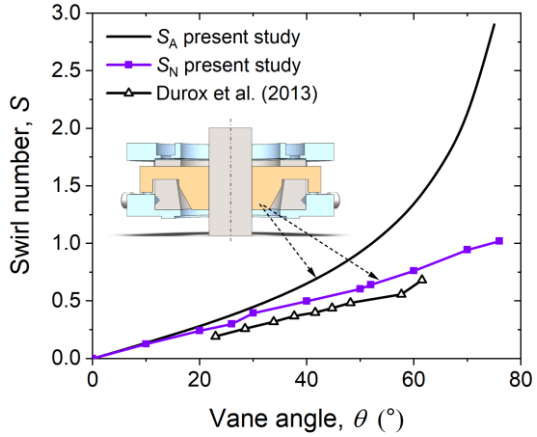

Fig. 2. The algebraic swirl number S_A, numerical swirl number S_N of the present axial swirler, and experimental measured swirl number of Durox's radial swirler [23] versus vane angles.

Simulations of non-reactive swirl flow

To evaluate the performance of the swirler and obtain a more precise swirl number, we utilized the SolidWorks Flow Simulation package [24] to conduct a numerical simulation of the non-reacting flow field in the swirl burner. The simulation package employs the modified k-ε turbulence model with damping functions proposed by Lam and Bremhorst [25] to model the three-dimensional velocity and pressure fields, making it suitable for turbulent flow cases.

Figure 3 illustrates the slice of the simulated velocity field at $\theta = 52°$ and 76°. The flow structure undergoes significant changes as θ increases from 52° to 76°. At θ around 52°, a recirculation zone forms in the central area of the quartz tube. The central and corner recirculation zones are clearly visible in Fig. 3 and are typical characteristics of swirling flow [9, 26]. When θ is adjusted to its maximum value, the central recirculation zone recedes towards the injector's exit, and its size becomes much larger than that at $\theta = 52°$. At this very large θ, the enhanced central recirculation zone reduces the size of the corner recirculation zone, but the recirculation velocity in the corner recirculation zone increases.

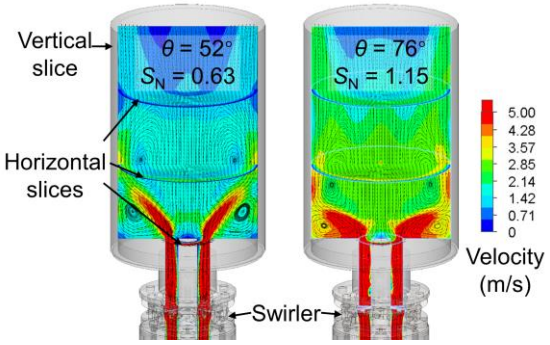

Fig. 3. Simulated swirling flow structures at vane angles $\theta = 52°$, and 76°.

Numerical simulation offers comprehensive velocity information of the swirling flow. We chose the simulation results at the injector's exit, the lowest horizontal slice in Fig. 3, to evaluate the swirl intensity. Since the contribution of the pressure term to the swirl number is much smaller than that of the velocity term in the current adjustable axial swirler [21], disregarding the pressure term leads to a negligible decrease in the swirl number. Substituting the simulated velocity distributions into Eq. (1) results in the numerically derived swirl number (S_N) of the current swirler, which is also plotted in Fig. 2. S_N almost linearly increases with the vane angle. When $\theta < 30°$, S_N closely aligns with the algebraic swirl number S_A. However, S_N becomes much lower than S_A at large θ. This discrepancy is due to the assumption in Eq. (2) that the axial and tangential velocities are uniform across the injector section. However, the velocity components have complex distributions at a high degree of swirl, which causes the difference between S_A and the numerical/experimental derived swirl number, as discussed in [8, 23]. Furthermore, Fig. 2 also displays the experimentally measured swirl number of an adjustable radial swirler developed in [23]. The two swirlers exhibit a similar slope versus vane angle, but the swirl number of the present swirler is slightly larger. This demonstrates that the adjustable axial swirler can generate a broad range of swirl intensities.

In this study, the vane angle was set utilizing the numerically calculated swirl number S_N. The swirl numbers 0.6 and 1.0 were selected as they are both substantial enough to establish a central recirculation zone for enhancing flame stability but produce noticeable distinctions in the swirl flow [26].

Sampling and optical methods

In this work, a variety of experimental measurements were conducted, including time-averaged broadband e, NO emissions, and PLIF. A DSLR camera (Sony α7RIVa) was utilized to capture time-averaged broadband flame images. NO

concentrations in the exhaust gases were obtained through the use of a quartz probe (2-mm ID and 4-mm OD) with a sonic orifice (~0.5 mm) and a Testo 350 analyzer. Considering the good radial uniformity of NO at the outlet of the quartz tube, NO was sampled at the burner centerline. The sampled gas was dried by two water separators upstream of the analyzer, and then analyzed by NO replacement sensor. These measurements were repeated three to four times for each test condition, and the standard deviation was used to estimate the experimental uncertainty. The NO concentrations were corrected for a 15% oxygen content to ensure fair comparisons [27].

The spatial distributions of NO and OH within the flame were imaged using PLIF. The NO-PLIF system comprises an Nd:YAG laser (Continuum Powerlite DLS9010) pumping a tunable dye laser (Continuum ND6000+UVT) to produce a UV laser at ~236 nm [28] with an energy output of ~1.5 mJ/pulse. The laser beam was expanded to a vertically oriented 60-mm high and ~0.2-mm laser sheet. The laser wavelength was precisely adjusted to excite NO in the (0–1) band of the $A^2\Sigma^+ - X^2\Pi$ transition at 235.85 nm. When the temperature is lower than 2500 K, the Boltzmann population fraction of NO at this transition increases monotonically with increasing temperature. The NO-PLIF signal was captured by an intensified CCD camera (Princeton PI-MAX4) equipped with a UV lens. A long-pass filter was used to collect the fluorescence of (2,0) and (3,0) bands above 244 nm but suppress scattered light. The gate time was set to 200 ns to suppress flame luminosity. The signal-to-noise ratio for the NO-PLIF signal is ~5. A total of 200 images were recorded at a rate of 10 Hz for each experimental condition.

The OH-LIF system comprises a high-speed laser (Edgewave IS 2002L) pumping a tunable dye laser (Sirah Credo) to produce a laser at ~283 nm. The output power was ~2.5 W. This laser beam was expanded to a 100-mm high and ~0.2-mm wide laser sheet. The OH-PLIF signal was collected by an intensified high-speed CMOS camera (LaVision HighSpeedStar coupled to HighSpeed IRO) equipped with a UV lens and a high-transmission band-pass filter centered at 310 nm (LaVision 1108760). The gate time was also set to 200 ns. A total of 1000 images were recorded at a frame rate of 10 kHz for each condition. It should be noted that NO- and OH-PLIF measurements were not conducted simultaneously.

Results and Discussion

Characterization of flame structure and NO emissions

The effect of varying swirl numbers on flame images is depicted in Fig. 4. In order to extract the flame luminescence features on a slice, an inverse Abel transformation was performed. Given that the flame image comprises red, green, and blue components, the Abel inversion of each color component was separately obtained and then combined.

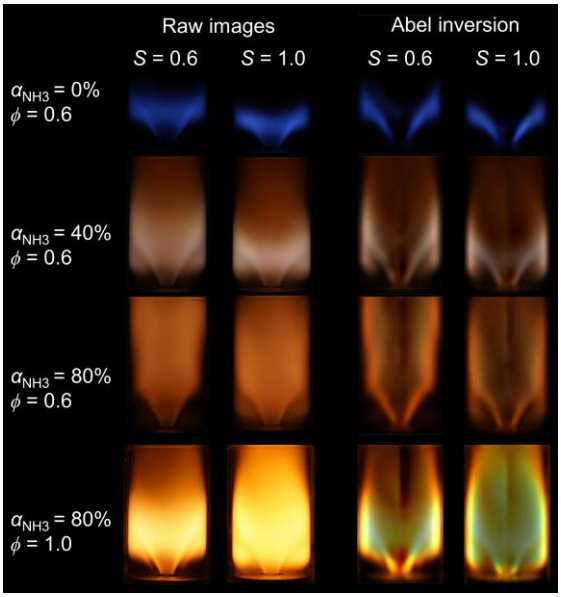

Fig. 4. Time-averaged broadband images and the inverse Abel transformed images of ammonia-methane-air premixed flame under swirl numbers of 0.6 and 1.0.

In Fig. 4, as the swirl number increases from 0.6 to 1.0, the overall hue of the flame remains unchanged. However, the length and structure of the flame are affected by the altered flow structures. On the one hand, increasing the swirl number causes the flame to become more compact, resulting in a decrease in flame length for $\alpha_{NH3} \leq 80\%$ and $\phi = 0.6$. On the other hand, a strong swirl enhances reactions in the central and corner recirculation zones, leading to the observation of luminous yellow/orange hues in the corner recirculation zones for $\alpha_{\mathrm{NH3}} = 80\%$ and $S = 1.0$.

Figure 5 illustrates the results of NO emission measured at the outlet of the quartz tube. It is observed that the exhaust gas of ammonia-methane-air flames can contain up to several thousands of ppmvd of NO, particularly when ϕ is around 0.7/0.8 and α_{NH3} increases up to 30/40%.

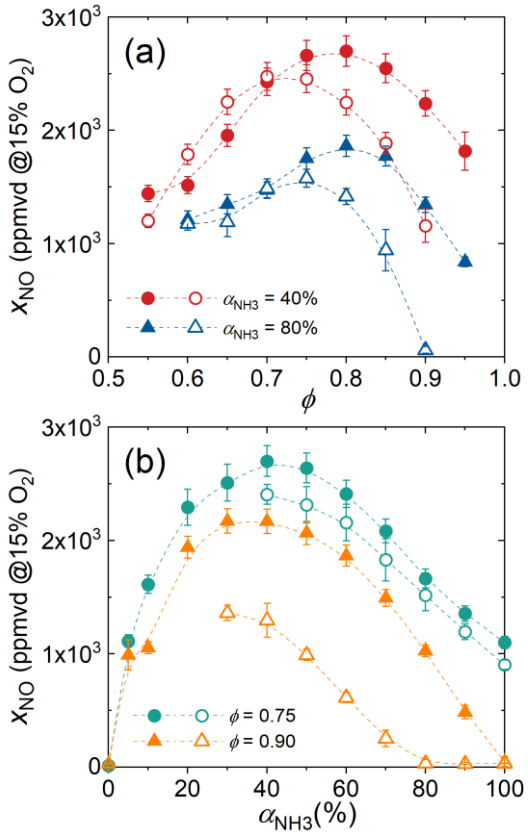

Fig. 5. Measured NO emissions versus (a) equivalence ratio and (b) ammonia volume fraction. The solid and open symbols represent the measurement for $S = 0.6$ and 1.0, respectively.

In contrast to the previously studied impact of residence time on NOx emission [17], this study focuses on the effect of varying swirl intensity on NO emissions. By comparing the NO emission at $S = 0.6$ and 1.0 in Fig. 5(a), it can be seen that changing the swirl number can significantly decrease the concentration of NO in the products at $\phi \geq 0.75$. In Fig. 5(b), it is evident that the flame at $\phi = 0.9$ and $\alpha_{NH3} \geq 80\%$ can decrease NO emissions by nearly a hundredfold, highlighting the powerful impact of swirl strength on NO emissions. However, this trend weakens at $\phi \leq 0.75$ and even exhibits the opposite behavior for $\alpha_{NH3} = 0.4$. The reason behind these contrasting trends in NO emissions is discussed in Section 3.3.

Moreover, it is necessary to note that N_2O is also a significant pollutant in ammonia combustion, as it has a higher global warming potential than carbon dioxide. However, N_2O formation is primarily observed in very lean ammonia flames with an equivalence ratio of less than 0.5. In the case of the present study, N_2O emissions at $\phi \geq 0.75$ are minimal and not significantly affected by swirling intensity.

The rapid formation of NO when burning ammonia blends has been demonstrated by measuring instantaneous NO- and NH- PLIF images in [29]. This implies that the reaction zone is the main region determining NO formation. Figure 6 illustrates the time-averaged NO- and OH-PLIF images measured in the main reaction zone (MRZ) over vast ranges of ϕ and α_{NH3}. The vertical luminous lines in the NO-PLIF image are interference fluorescence signals caused by the refraction effect of the curved wall of the quartz tube. Across the board, trends of NO-LIF intensity with S, ϕ, and α_{NH3} correspond with that of OH-PLIF. A positive correlation between NO- and OH-LIF intensities has been verified. As previously discussed in [17], NO is primarily produced through fuel NOx pathways, where OH radicals promote the oxidation of NH and NH_2 to form NO through an HNO intermediate route [30].

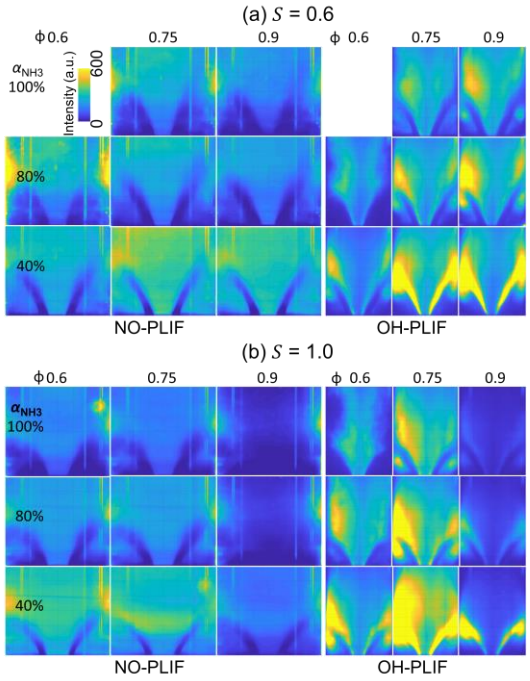

Fig. 6. Time-averaged NO- and OH- PLIF images near the nozzle for swirl number S = 0.6 (a) and S = 1.0 (b). The colormap is normalized to a fluorescence intensity value of 600 to better show differences in fluorescence images.

Distributions of PLIF intensities

Figures 7 and 8 compare the integrated intensities of NO- and OH-PLIF at various heights. The NO-PLIF intensity rapidly rises within the MRZ and remains uniform in the post-flame zone (PFZ). It does not vary significantly as the height above the nozzle increases. This is very different from the exponential decrease in OH-PLIF intensity in the PFZ resulting from OH super-equilibrium.

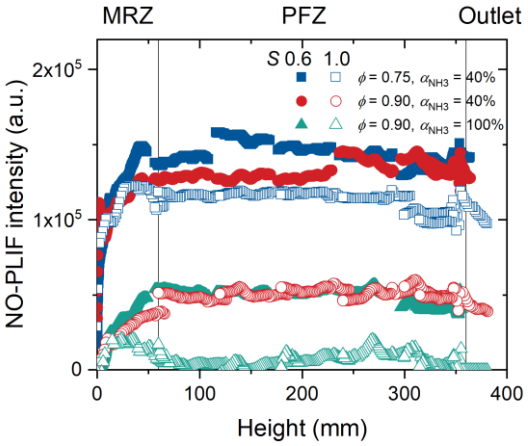

Fig. 7. Horizontally integrated PLIF intensities of NO at different heights above the nozzle. The solid and open symbols represent the NO fluorescence for $S = 0.6$ and 1.0, respectively.

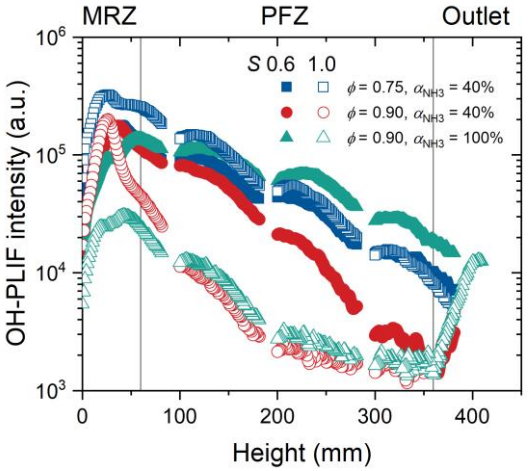

Fig. 8. Horizontally integrated PLIF intensities of OH at different heights above the nozzle. The solid and open symbols represent the OH fluorescence for $S = 0.6$ and 1.0, respectively.

The fact that the NO-PLIF signal downstream of the flame remains largely unchanged indicates that its intensity can potentially serve as an indicator of NO concentration. We have measured the NO emission at the outlet of the quartz tube in Section 3.1. By examining the correlation between the NO-LIF signal intensity and NO emissions, we can assess the feasibility of utilizing NO-LIF to characterize NO concentration. Therefore, we examined the correlation between the NO-PLIF plateau and the sampled NO mole fraction by the Testo system [17]. The measured NO concentration and NO-PLIF signal intensity of the same flame are depicted as the abscissa and ordinate, respectively. Figure 9 illustrates a positive linear relationship between the NO-PLIF plateau intensity and the measured NO mole fraction at the quartz tube's outlet. Although the exhaust gas temperature downstream of the MRZ gradually decreases as a result of heat loss as it flows towards the outlet, however, the exhaust gas temperature does not significantly affect the NO-PLIF intensity at different heights in Fig. 7. Consequently, the NO-PLIF plateau can be used as an approximate estimate of the NO concentration in this burner. This estimation provides valuable insights into the characteristics of NO generation from the reaction layer and its downstream distribution. It complements the single-point NO measurement obtained through the sampling method, thereby enhancing our understanding of the impact of swirl intensity on NO emissions.

However, it is important to note that the basis for adopting this correlation is the weak dependence of NO-PLIF intensity on temperature changes downstream of the flame. If other NO-LIF exciting transitions exhibit strong temperature dependence or collisional quenching significantly impacts the NO-LIF signal intensity, the relationship between the NO-LIF signal and NO concentration will need to be re-evaluated.

As seen in Fig. 7, increasing S from 0.6 to 1.0 reduces the NO-PLIF intensities, particularly for $\phi = 0.9$ [17]. The reduction primarily occurs within the MRZ. Additionally, the same NO mole fraction in Fig. 9 corresponds to a lower NO-PLIF intensity at higher S. This means that the exhaust temperature at $S = 1.0$ is lower because the Boltzmann population fraction of NO increases monotonically with increasing temperature [31]. The increased heat loss caused by enhanced recirculation close to the nozzle is likely the reason for the lower flame temperature at higher S.

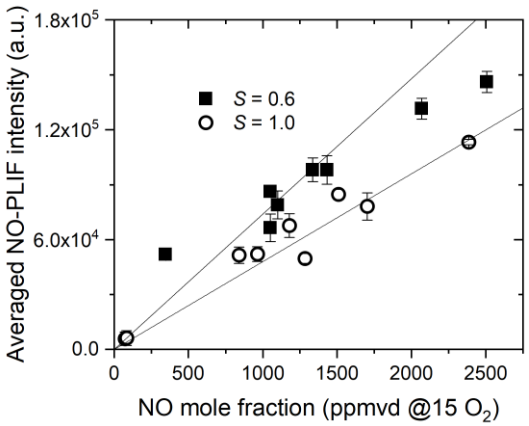

Fig. 9. Averaged NO-PLIF intensities in the plateau versus the sampled NO mole fraction at the outlet.

NO emissions with heat insulation

The analysis based on NO-PLIF measurements indicates that temperature may have a significant impact on NO production. Okafor et al. [18] discovered that wall heat loss hindered NO emission while studying ammonia-air single-stage flame. In

this study, to comprehend the direct influence of temperature changes on the NO emission of the ammonia-methane swirling flame, we insulated the quartz tube with a 30 mm thick insulation cotton layer and measured the NO emission concentration with the insulation layer for comparison with non-insulation NO emissions. Figure 10 illustrates the impact of thermal boundary conditions on NO emissions. To ensure that the flow conditions remain entirely consistent, we only measured the flame with a swirl number of $S = 1.0$.

When the heat insulation layer reduces heat loss and increases the temperature inside the quartz tube, the NO emission value significantly improves. When $\phi = 0.75$ and α_{NH3} is less than 1, the NO emissions can increase by nearly 1000 ppm. Although the increase in temperature can promote the formation of thermal NOx, the plateau of NO fluorescence in the high-temperature zone downstream of the flame in Fig. 7 indicates that thermal NOx did not significantly raise the NO concentration in this experiment. Thus, it can be inferred that the primary effect of temperature increase is to alter the concentration of active free radicals like OH, which subsequently affects NO emissions via the fuel-type NOx formation pathway.

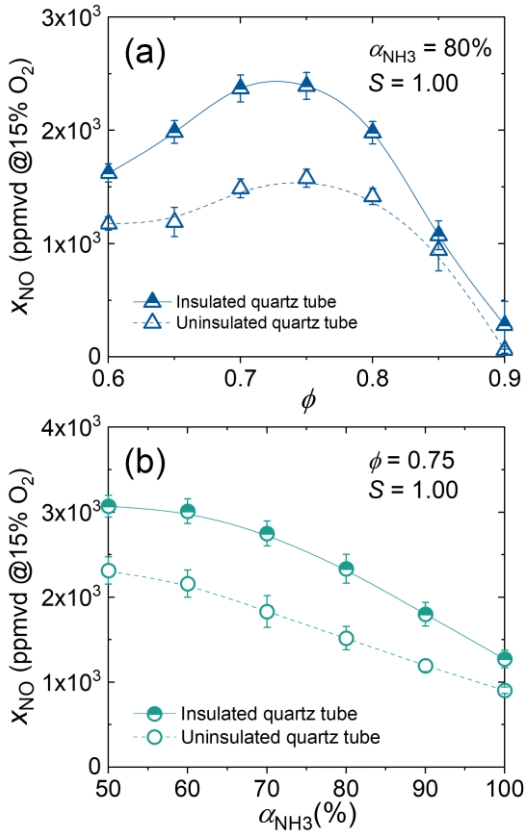

Fig. 10. Effect of heat insulation on NO emissions at varying equivalence ratios (a) and ammonia volume fractions (b).

Overall, based on NO emissions and PLIF measurements, we inferred temperature changes from NO-PLIF intensity differences. We also derived the change in NO emissions after changing the isolating condition. It is certain that the change of temperature under different swirl intensities can significantly affect the NO emission in the ammonia-methane flame. We also observed that there is a strong positive correlation between the intensity of OH-PLIF in the main reaction zone and the NO concentrations. Therefore, we infer that the change of the swirl intensity is likely to change the OH concentration by affecting the temperature, and then affect the formation of NO. Abundant reducing components, such as NHi (i = 1, 2, and 3), are key factors for this NO reduction mechanism to work.

Based on the above analysis of swirl intensity affecting NO emissions, we can better explain the experimental results observed in Figs. 5 to 8. In Fig. 5, increasing the swirl number significantly reduces the NO concentration at $\phi \geq 0.75$, but this reduction trend weakens at $\phi \leq 0.75$. The less affected NO emissions at lower ϕ values may be attributed to the fact that heat loss has less effect on flame temperature at $\phi \leq 0.75$, and the reducing components, i.e., NHi (i = 1, 2, and 3), are not abundant. Consequently, the NO produced in the flame for $\phi \leq 0.75$ is less sensitive to changes in swirl intensity.

In Fig. 8, the lower temperature at higher S in the MRZ hinders the formation of active OH radicals. As a result, increasing S exacerbates the decreasing rate of OH concentration. For $\phi = 0.9$ and $\alpha_{NH3} = 100\%$, the peak OH-PLIF intensity at $S = 1.0$ is five times lower than at $S = 0.6$. This greatly suppresses the formation of NO in the MRZ. The intense heat loss in the MRZ of pure ammonia flame significantly suppresses the reactions producing OH. The lower OH further slows down chemical reactions, including fuel-type NOx pathways. The re-increase of OH at the outlet in Fig. 8 confirms that incomplete combustion also contributes to the significant reduction of reactive OH and NO radicals at $\phi = 0.9$ and $\alpha_{NH3} = 100\%$. Figure 8 also shows that the integrated intensities of OH-PLIF peak at larger swirl intensity appear to be higher for the flames with $\phi = 0.75$ and 0.9 and $\alpha_{NH3} = 40\%$. Since the flame is more compact due to the increased swirl intensity, the distribution of OH is also more concentrated, which could make the peak of OH-PLIF intensity appear to be higher. Moreover, in this study, it is not feasible to establish a linear correlation between the signal intensity of OH-PLIF and the OH concentration. This is primarily due to the temperature-dependent characteristic of OH-LIF, which is not necessarily monotonic.

Conclusions

The emission characteristics of ammonia-methane-air premixed swirling flames were examined using a single-stage swirl burner. An adjustable axial swirler was employed to achieve a wide range of swirl numbers. As the swirl number increased from 0.6 to 1.0, the concentration of NO in exhaust gas was significantly reduced for $\phi = 0.90$ and $\alpha_{NH3} > 80\%$. NO/OH-PLIF analysis revealed that the formation of NO was primarily determined by the main reaction zone via the fuel-NOx pathway. The NO-PLIF intensity in the post-flame zone remained unchanged at different heights and can be used to estimate the NO concentration, though its correlation is affected by swirl intensity. The increased heat loss near the nozzle at higher swirl intensities reduces the flame temperature in the main reaction zone, inhibiting the formation of OH radicals and incomplete reactions under high α_{NH3}, ultimately resulting in low NO emissions. When designing the swirl flow structure of the ammonia flame in the actual combustion chamber, changing the swirl intensity may strongly impact NO emissions, and the influence of changing the swirl flow structure on the flame temperature is likely a key factor.

In the future, measuring the velocity and temperature fields of ammonia flames with varying swirl intensities will be crucial. This will facilitate a deeper understanding of the mechanisms by which turbulence-chemistry interaction and combustion temperature impact NOx emissions in ammonia combustion.

Acknowledgments

This research was supported by funding from King Abdullah University of Science and Technology (KAUST) (BAS/1/1425-01-01).

Conflicts of Interest

The authors declare no conflict of interest. The funders had no role in the design of the study; in the collection, analyses, or interpretation of data; in the writing of the manuscript, or in the decision to publish the results".

References

1. Valera-Medina A, Xiao H, Owen-Jones M, David WIF, Bowen PJ. Ammonia for power. *Prog Energy Combust Sci.* 2018; 69: 63-102. DOI: https://doi.org/10.1016/j.pecs.2018.07.001.

2. Kobayashi H, Hayakawa A, Somarathne KKA, Okafor EC. Science and technology of ammonia combustion. *Proc Combust Inst.* 2019; 37(1): 109-133. DOI: https://doi.org/10.1016/j.proci.2018.09.029.

3. da Rocha RC, Costa M, Bai X-S. Chemical kinetic modelling of ammonia/hydrogen/air ignition, premixed flame propagation and NO emission. *Fuel*. 2019; 246: 24-33. DOI: https://doi.org/10.1016/j.fuel.2019.02.102.

4. Pochet M, Dias V, Moreau B, Foucher F, Jeanmart H, Contino F. Experimental and numerical study, under LTC conditions, of ammonia ignition delay with and without hydrogen addition. *Proc Combust Inst.* 2019; 37(1): 621-629. DOI: https://doi.org/10.1016/j.proci.2018.05.138.

5. Zhang M, Wei X, Wang J, Huang Z, Tan H. The blow-off and transient characteristics of co-firing ammonia/methane fuels in a swirl combustor. *Proc Combust Inst.* 2021; 38(4): 5181-5190. DOI: https://doi.org/10.1016/j.proci.2020.08.056.

6. Hayakawa A, Arakawa Y, Mimoto R, Somarathne KKA, Kudo T, Kobayashi H. Experimental investigation of stabilization and emission characteristics of ammonia/air premixed flames in a swirl combustor. *Int J Hydrogen Energy*. 2017; 42(19): 14010-14018. DOI: https://doi.org/10.1016/j.ijhydene.2017.01.046.

7. Ariemma GB, Sorrentino G, Ragucci R, de Joannon M, Sabia P. Ammonia/Methane combustion: Stability and NOx emissions. *Combust Flame.* 2022; 241: 112071. DOI: https://doi.org/10.1016/j.combustflame.2022.112071.

8. Candel S, Durox D, Schuller T, Bourgouin J-F, Moeck JP. Dynamics of swirling flames. *Ann Rev Fluid Mech.* 2014; 46(1): 147-173. DOI: https://doi.org/10.1146/annurev-fluid-010313-141300.

9. Wang G, Liu X, Xia X, Wang S, Qi F. Dynamics of periodically-excited vortices in swirling flames. *Proc Combust Inst.* 2020; 38(4): 6183-6191. DOI: https://doi.org/10.1016/j.proci.2020.06.308

10. Wang G, Liu X, Li L, Chen ZX, Qi F. Investigation on the flame front and flow field in acoustically excited swirling flames with and without confinement. *Combust Sci Tech.* 2022; 194(1): 130-143. DOI: https://doi.org/10.1080/00102202.2019.1678388.

11. Claypole TC, Syred N. The effect of swirl burner aerodynamics on NOx formation. *Symp (Int) Combust.* 1981; 18(1): 81-89. DOI: https://doi.org/10.1016/S0082-0784(81)80013-6.

12. Zhou LX, Chen XL, Zhang J. Studies on the effect of swirl on no formation in methane/air turbulent combustion. *Proc Combust Inst.* 2002; 29(2): 2235-2242. DOI: https://doi.org/10.1016/S1540-7489(02)80272-3.

13. Rashwan SS. The Effect of Swirl Number and Oxidizer Composition on Combustion Characteristics of Non-Premixed Methane Flames. *Energy Fuels*. 2018; 32(2): 2517-2526. DOI: https://doi.org/10.1021/acs.energyfuels.8b00233.

14. Hosseini AA, Ghodrat M, Moghiman M, Pourhoseini SH. Numerical study of inlet air swirl

intensity effect of a Methane-Air Diffusion Flame on its combustion characteristics. *Case Studies Thermal Eng.* 2020; 18: 100610. DOI: https://doi.org/10.1016/j.csite.2020.100610.

15. Valera-Medina A, Marsh R, Runyon J, Pugh D, Beasley P, Hughes T, Bowen P. Ammonia–methane combustion in tangential swirl burners for gas turbine power generation. *Appl Energy*. 2017; 185: 1362-1371. DOI: https://doi.org/10.1016/j.apenergy.2016.02.073.

16. Jójka J, Ślefarski R. Emission characteristics for swirl methane–air premixed flames with ammonia addition. *Energies*. 2021; 14(3): 662. DOI: https://doi.org/10.3390/en14030662.

17. Wang G, Guiberti TF, Cardona S, Jimenez CA, Roberts WL. Effects of residence time on the NOx emissions of premixed ammonia-methane-air swirling flames at elevated pressure. *Proc Combust Inst.* 2022; 39: 1-12. DOI: https://doi.org/10.1016/j.proci.2022.07.141.

18. Okafor EC, Tsukamoto M, Hayakawa A, Somarathne KDKA, Kudo T, Tsujimura T, Kobayashi H. Influence of wall heat loss on the emission characteristics of premixed ammonia-air swirling flames interacting with the combustor wall. *Proc Combust Inst.* 2021; 38(4): 5139-5146. DOI: https://doi.org/10.1016/j.proci.2018.07.083.

19. Boyette WR, Elbaz AM, Guiberti TF, Roberts WL. Experimental investigation of the near field in sooting turbulent nonpremixed flames at elevated pressures. *Exp Thermal Fluid Sci.* 2019; 105: 332-341. DOI: https://doi.org/10.1016/j.expthermflusci.2019.04.008.

20. Chigier NA, Bee´r JM. Velocity and Static-Pressure Distributions in Swirling Air Jets Issuing From Annular and Divergent Nozzles. *J Basic Eng.* 1964; 86(4): 788-796. DOI: https://doi.org/10.1115/1.3655954.

21. Vignat G, Durox D, Candel S. The suitability of different swirl number definitions for describing swirl flows: Accurate, common and (over-) simplified formulations. *Prog Energy Combust Sci*. 2022; 89: 100969. DOI: https://doi.org/10.1016/j.pecs.2021.100969.

22. Syred N, Bekr JM. Combustion in Swirling Flows : A Review. *Combust Flame.* 1974; 201: 144- DOI: https://doi.org/10.1016/0010-2180(74)90057-1.

23. Durox D, Moeck JP, Bourgouin J-F, Morenton P, Viallon M, Schuller T, Candel S. Flame dynamics of a variable swirl number system and instability control. *Combust Flame.* 2013; 160(9): 1729-1742. DOI: http://doi.org/10.1016/j.combustflame.2013.03.004.

24. Ivanov AV, Trebunskikh TV, Platonovich *The measured NO concentration* , Validation Methodology for Modern CAD-Embedded CFD Code: from Fundamental Tests to Industrial Benchmarks, 2020.

25. Lam CKG, Bremhorst K. A Modified Form of the k-ε Model for Predicting Wall Turbulence. *J Fluids Eng.* 1981; 103(3): 456-460. DOI: https://doi.org/10.1115/1.3240815.

26. Syred N. A review of oscillation mechanisms and the role of the precessing vortex core (PVC) in swirl combustion systems. *Prog Energy Combust Sci.* 2006; 32(2): 93-161. DOI: http://dx.doi.org/10.1016/j.pecs.2005.10.002.

27. Baukal CE, Eleazer PB. Quantifying NOx for Industrial Combustion Processes. *J Air Waste Manag Assoc.* 1998; 48(1): 52-58. DOI: https://doi.org/10.1080/10473289.1998.1046366.

28. Thompson BA, Reeves RR, Harteck P. Ultraviolet absorption coefficients of CO_2, CO, O_2, H_2O, N_2O, NH_3, NO, SO_2, and CH_4 between 1850 and 4000 A. *J Geophys Res* (1896-1977). 1963; 68(24): 6431-6436. DOI: https://doi.org/10.1029/JZ068i024p06431.

29. Wang G, Shi H, Roberts WL, Guiberti TF. Simultaneous imaging of NO and NH in an ammonia-hydrogen-nitrogen flame using a single dye laser. *Combust Flame*. 2022; 245: 112355. DOI: https://doi.org/10.1016/j.combustflame.2022.112355.

30. Xiao H, Valera-Medina A, Bowen PJ. Study on premixed combustion characteristics of co-firing ammonia/methane fuels. *Energy.* 2017; 140: 125-135. DOI: https://doi.org/10.1016/j.energy.2017.08.077.

31. Wang G, Tang H, Yang C, Magnotti G, Roberts WL, Guiberti TF. Quantitative laser-induced fluorescence of NO in ammonia-hydrogen-nitrogen turbulent jet flames at elevated pressure. *Proc Combust Inst.* 2022; 39: 1-10. DOI: https://doi.org/10.1016/j.proci.2022.08.097.